Materials Research. 2016; 19(2): 370-378
DOI:http://dx.doi.org/10.1590/1980-5373-MR-2015-0104

Microstructural Evolution and Mechanical Properties in Directionally Solidified Sn–10.2 Sb Peritectic Alloy at a Constant Temperature Gradient

Elif Yılmaz[a], Emin Çadırlı[b]*, Emine Acer[c], Mehmet Gündüz[d]

[a]*Kayseri Vocational High School, Erciyes University, Kayseri, Turkey*
[b]*Department of Physics, Faculty of Arts and Sciences, Niğde University, Niğde, Turkey*
[c]*Department of Physics, Institute of Science, Erciyes University, Kayseri, Turkey*
[d]*Department of Physics, Faculty of Sciences, Erciyes University, Kayseri, Turkey*

Received: February 6, 2015; Revised: October 20, 2015; Accepted: December 22, 2015

The Sn–10.2 Sb (mass fraction) peritectic alloy was prepared using a vacuum melting furnace and a hot filling furnace. The samples were directionally solidified upwards at steady state conditions with a constant temperature gradient (G=4.5±0.2 K. mm^{-1}) under different growth velocities (V=13.3–266.7 µm. s^{-1}) in a Bridgman-type directional solidification apparatus. The effects of the growth velocity (V) on the dendritic spacings were investigated. Primary dendrite arm spacing (PDAS) of α phase in directionally solidified Sn–10.2 Sb peritectic alloy was measured on the longitudinal and transverse sections of 4 mm diameter cylindrical samples. Secondary dendrite arm spacing (SDAS) was measured on the longitudinal section. The experimental results show that the measured PDAS (λ_{1L}, λ_{1T}) and SDAS (λ_2) decrease with increasing growth velocity. The dependence of PDAS, SDAS, microhardness (HV) and compressive strength (σ_c) on the growth velocity were determined by using a linear regression analysis. The experimental results were compared with the previous experimental results and the results of the experimental models.

Keywords: *Solidification, Microstructure, Dendrite arm spacings, Peritectic alloy, Microhardness, Compressive strength Sn-Sb alloy*

1. Introduction

Peritectic solidification has attracted more attention in experimental and theoretical studies[1] since many technologically important materials are peritectic, such as Sn–Cd[2,3], Sn–Sb[4,5], Sn-Ag[6], Sn–Bi–Zn[7], Zn–Cu[8,9], Zn–Ag[10] lead-free soldering materials, high temperature intermetallics Ti–Al[11], Ni–Al[12], HF–B[13], superconducting materials YBCO[14], magnetic materials Nd–Fe–B[15], and structural materials Fe–Ni[16,17] and Fe–Cr–Ni[18]. Many interesting microstructures have been found during directional solidification of peritectic alloys, which have drawn much attention since the last four decades[4]. In the solidification of these alloys, a dendrite structure is the commonly encountered pattern. The microstructural scales involving the primary dendrite arm spacing (PDAS) and the secondary dendritic arm spacing (SDAS) have been carried out in directional solidification of various peritectic alloys, including Pb–Bi[19], Zn–Cu[19] and Nd–Fe–B[20]. In fact, PDAS and SDAS in the solidification microstructure determine the final physical properties of peritectic alloys. Therefore, it is of great significance to control the peritectic solidification by different techniques (Bridgman method[6,7], Forced Crucible Rotation[21], Bridgman-Stockbarger[22], Ultrasonic Vibration [5,23], Temperature Gradient Zone Melting[24]).

Tin–antimony alloys are important materials in the industry for their use in die casting alloys, high temperature lead–free solders, manufacture of cable sheathing and battery grids, and in manufacturing acidic accumulators[25,26]. It is usually applied in the industry as a sliding material such as the bearing babbit alloy. The Sn-Sb peritectic alloy has widespread applications, and is valuable in the industry[27]. Recently, the study by Rosa et al.,[28] has shown that improvement in cell size and corrosion resistance depends on the cooling rate imposed during directional solidification of the Sb–Pb alloy.

The investigations of mechanical properties of Sn–Sb alloys are crucial for many industrial applications. However, the effects of growth velocity on the microstructure and mechanical properties of the Sn–10.2 Sb peritectic alloy have not been investigated in a systematic manner. Therefore, the aim of the present work is to study the effect of growth velocity on PDAS, SDAS, microhardness (HV), and compressive strength (σ_c) for a directionally solidified Sn–10.2 Sb peritectic alloy using the Bridgman method at a constant temperature gradient (G=4.5 K. mm^{-1}), and to compare the results with the previous experimental results for similar alloy systems.

2. Experimental Procedure

2.1. Alloy preparation, directional solidification and metallographic processes

The master alloy Sn–10.2 Sb (*all compositions are in wt.% unless otherwise noted*) was prepared by melting weighed quantities of (≥99.99 wt.%) Sn and (≥99.99 wt.%) Sb metals in a graphite crucible (170 mm length, 30 mm inner diameter,

*e-mail: ecadirli@gmail.com

and 40 mm outer diameter), which was placed in a vacuum melting furnace, and the metals were completely melted, taking into account the phase diagram[29] as shown Figure 1. After allowing time for the melt to become homogeneous, the molten master alloy was stirred and quickly poured into the graphite crucibles (ID: 4 mm, OD: 6.4 mm and L: 200 mm) which were placed in a hot filling furnace and then lowered to the cold region of the furnace. The samples were directionally frozen from the bottom to the top to ensure that the samples were full to the brim. One of the prepared samples was positioned in a Bridgman–type furnace. After stabilizing the thermal conditions in the furnace under an argon atmosphere, the sample was withdrawn downwards by approximately 90–100 mm with a known pulling rate by means of a synchronous motor and the sample rapidly quenched. The block diagram of the experimental set up is shown in Figure 2. Samples were solidified under steady state conditions with different V (13.3–266.7 μm. s^{-1}) at a constant G (4.5 K. mm^{-1}) in order to investigate the effect of V on PDAS, SDAS, HV and σ_c.

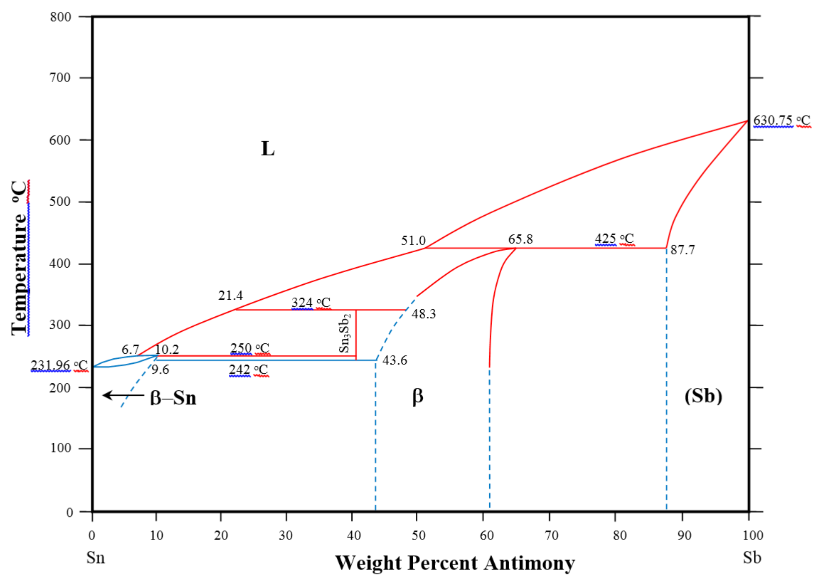

Figure 1. The Sn-Sb phase diagram[29]

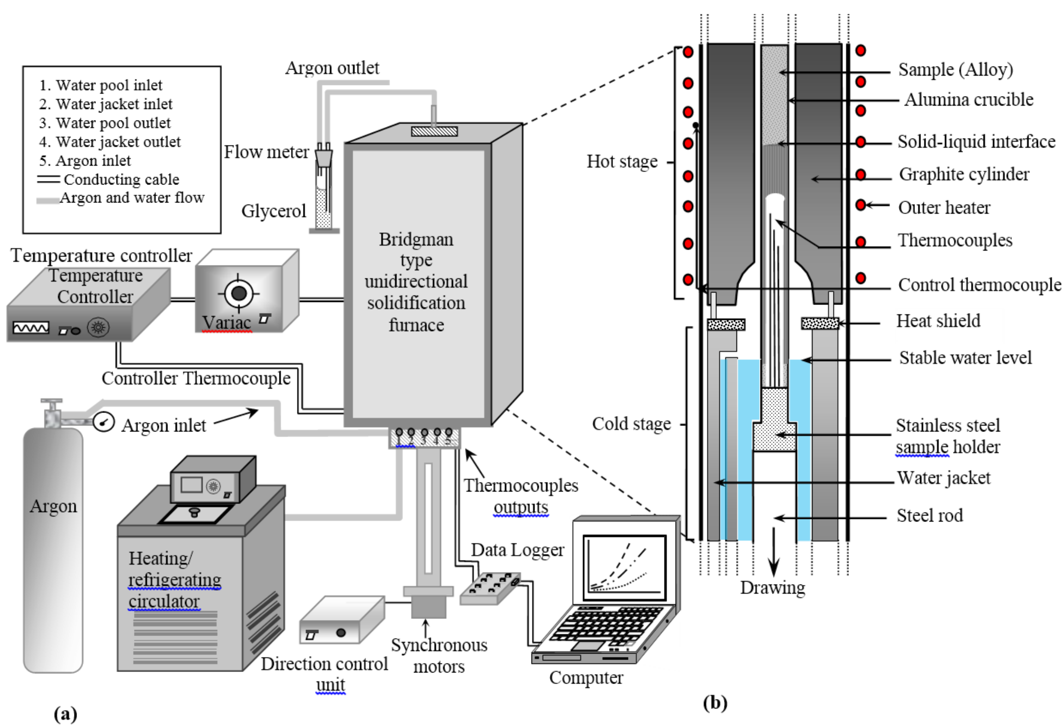

Figure 2. (a) Block diagram of the experimental setup, (b) The details of the Bridgman–type directional solidification furnace

2.2. Measurement of solidification processing parameters (G and V)

The temperature of the Bridgman–type furnace was controlled by a 0.5 mm insulated K-type thermocouple placed between the heating element and alumina tube. The temperature could be controlled to about ±0.1 K during the run. Three insulated K–type 0.5 mm diameter thermocouples with known distances were placed in alumina crucibles which were parallel to the direction of heat flow inside the graphite cylinder (see Figure 2). All of the leads were connected to a data logger interfaced with a computer and the temperature data recorded simultaneously. When the third thermocouple was at the solid–liquid interface and then the first and the second thermocouples in the liquid, their temperatures were used to obtain the temperature gradient *G*. G was also obtained from the recorded cooling rates ($\dot{T} = G\,V$). Both results were similar. *G* could be kept constant during the run by keeping the temperature of the cooler part and the hotter part of the furnace constant, and the distance between them stable. The positions of the thermocouples were measured by electronic calipers having an accuracy of ±0.02 mm after quench. Careful experimental measurements showed that the pulling rates of the samples were equal to the value of the growth velocities[30]. The solidification time and solidified distance were also measured for the run and their ratio gives the growth velocity. The error in the *G* and *V* measurements has been calculated to be about 4%.

2.3. Metallographic examination

The unidirectionally grown quenched sample was removed from the alumina crucible, then ground to observe the solid-liquid interface. The longitudinal section of the sample (10 mm), which included the quenched interface, was separated from the sample and set in the cold mounting resin. The longitudinal and transverse sections of this part were ground and polished using diamond paste to a 1 µm finish and etched within the solution of 100 ml H_2O and 10 g CrO_3 to reveal the microstructure. The microstructures of the samples were investigated by using Olympus BH–2 optical microscopy with LG Honeywell CCD camera.

2.4. Measurement of primary and secondary dendrite arm spacing

The primary dendrite arm spacing, PDAS (λ_1), was measured on the longitudinal and transverse sections of each sample by using the linear intercept method[30-32]. In the linear intercept method, λ_{1L} is obtained on the longitudinal section by measuring the distance between adjacent dendrite tips. Although λ_1 is independent of the distance behind the quenched interface, to be more precise, the λ_{1T} measurements on the transverse sections were taken on the plane ≤ 500 µm just behind the tips. The total 50–250 λ_1 were measured using the mean linear intercept method on the longitudinal and transverse sections, depending on the growth conditions. The secondary dendrite arm spacing λ_2 was measured on the longitudinal sections of the samples from the initial adjacent side branches of primary dendrites. Values of λ_2 data reported here were averaged over the 25–50 λ_2 measurements depending on the growth conditions. It has been found that a standard deviation is approximately 5% for λ_1 and λ_2 measurements.

2.5. Measurement of microhardness (HV) and compressive strength (σ_c)

Microhardness measurements in the present work were made with a DuraScan 20 semiautomatic Microhardness test device using a 300 g load and a dwell time of 10 s. Ten measurements were taken from the longitudinal and transverse sections of each sample. The average values were calculated from these microhardness values. Some errors were inevitable during the microhardness measurements. These errors were owing to factors such as surface quality, inhomogeneities in the microstructure, and the ambiguity of the traces. The error in the microhardness measurements has been calculated to be approximately 5%.

The measurements of the compressive tensile strength were made at room temperature with a Shimadzu AG-IS universal testing machine. Cylindrical compressive test samples with a diameter of 4 mm and gauge length of 6 mm were prepared from the directionally solidified rod samples under different growth velocities. The compressive axis was parallel to the growth direction of the sample. The compressive tests were repeated three times and the average value was taken. It has been found that the standard deviation was approximately 5%.

3. Results and Discussion

3.1. Composition analysis of the phases (EDS Analysis)

EDS analysis was performed to determine the composition of the phases in the Sn–10.2 Sb (mass fraction) peritectic alloy at 20 keV using X-ray lines. According to the EDS analysis results shown in Figure 3, three different phases (dark gray quenched liquid phase, light gray dendritic matrix phase, and white SnSb intermetallic phase) grew during the directional solidification of Sn–10.2 Sb alloy. The composition of the dendritic matrix phase (β–Sn) was Sn–10.16 Sb (wt.%), and that of the dark gray quenched liquid phase was Sn–6.39 Sb (wt.%). Also, the white phase (SnSb intermetallic phase) was Sn–43.76 Sb (wt.%). These determined compositions are very close to values of nominal compositions (Figure 1).

3.2. The effect of growth velocity on dendritic spacings

The Sn–10.2 Sb peritectic alloy was directionally solidified at steady state conditions with different growth velocities (*V*=13.3–266.7 µm. s^{-1}) at a constant temperature gradient (*G*=4.5 K. mm^{-1}). The optical micrographs of longitudinal and transverse sections of the directionally solidified Sn–10.2 Sb peritectic alloy prepared under different solidification parameters are given in Figure 4. As seen in Figure 4, the microstructure is dendritic form. The PDAS was measured from the longitudinal and transverse sections and SDAS was measured from the longitudinal section of the samples grown at different *V*. As seen in Figure 5, an increase in growth velocity caused a decrease of the PDAS and SDAS at a constant temperature gradient (4.5 K. mm^{-1}). When the growth velocity was increased from 13.3 to 266.7 µm. s^{-1},

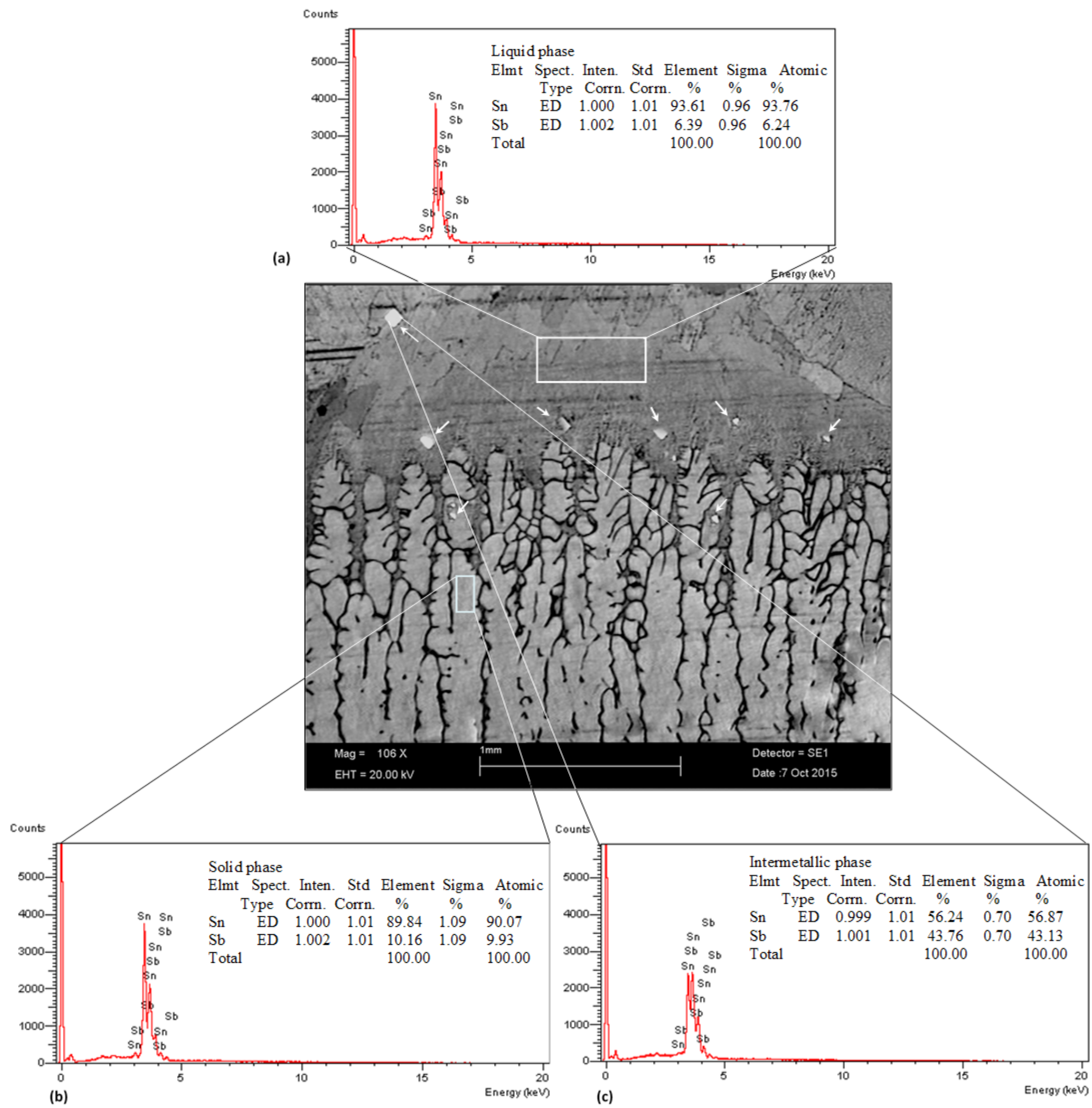

Figure 3. The chemical composition analysis of the Sn–10.2 Sb peritectic alloy (a) Dark gray phase (Sn-rich quenched liquid phase) (b) Light gray phase (β–Sn phase) (c) White phase (indicated by arrows) SnSb intermetallic phase

the λ_{IL} value decreased from 82.1 to 39.3 µm and the λ_{IT} value decreased from 78.1 to 36.2 µm. Similarly, when the growth velocity was increased from 26.7 to 266.7 µm. s^{-1}, the λ_2 value decreased from 40.4 to 15.3 µm. Secondary dendrite arms were not observed for 13.3 µm. s^{-1} growth velocity, because the microstructure is cellular or cellular–dendritic (see Figure 4). The dependency of λ_1 and λ_2 on V was determined by a linear regression analysis. From the experimental results, the relationship between microstructure parameters (λ_1, λ_2) and growth velocity (V) can be established as follows:

$$\lambda_{IL} = k_1 \ V^{-a} \tag{1a}$$

$$\lambda_{IT} = k_2 \ V^{-b} \tag{1b}$$

$$\lambda_2 = k_3 \ V^{-c} \tag{2}$$

where *a, b* and *c* are exponent values for the growth velocity, and k_1, k_2 and k_3 are constants which can be experimentally determined. According to Eqs. (1) and (2), PDAS and SDAS change with the growth velocity. The exponent values (*a*, *b*) of V were found to be 0.24 and 0.25 for λ_1 values obtained from longitudinal and transverse sections of samples respectively. Similarly, the exponent value (*c*) of V found to be 0.46 for λ_2 value was obtained from longitudinal sections of samples. The exponent values (*a*, *b* and *c*) and experimental constants (k_1, k_2 and k_3) are given in Table 1. The exponent values (0.24 and 0.25) of λ_1 are in agreement with the values 0.25, 0.23, 0.27, 0.26, 0.25 and 0.28 obtained

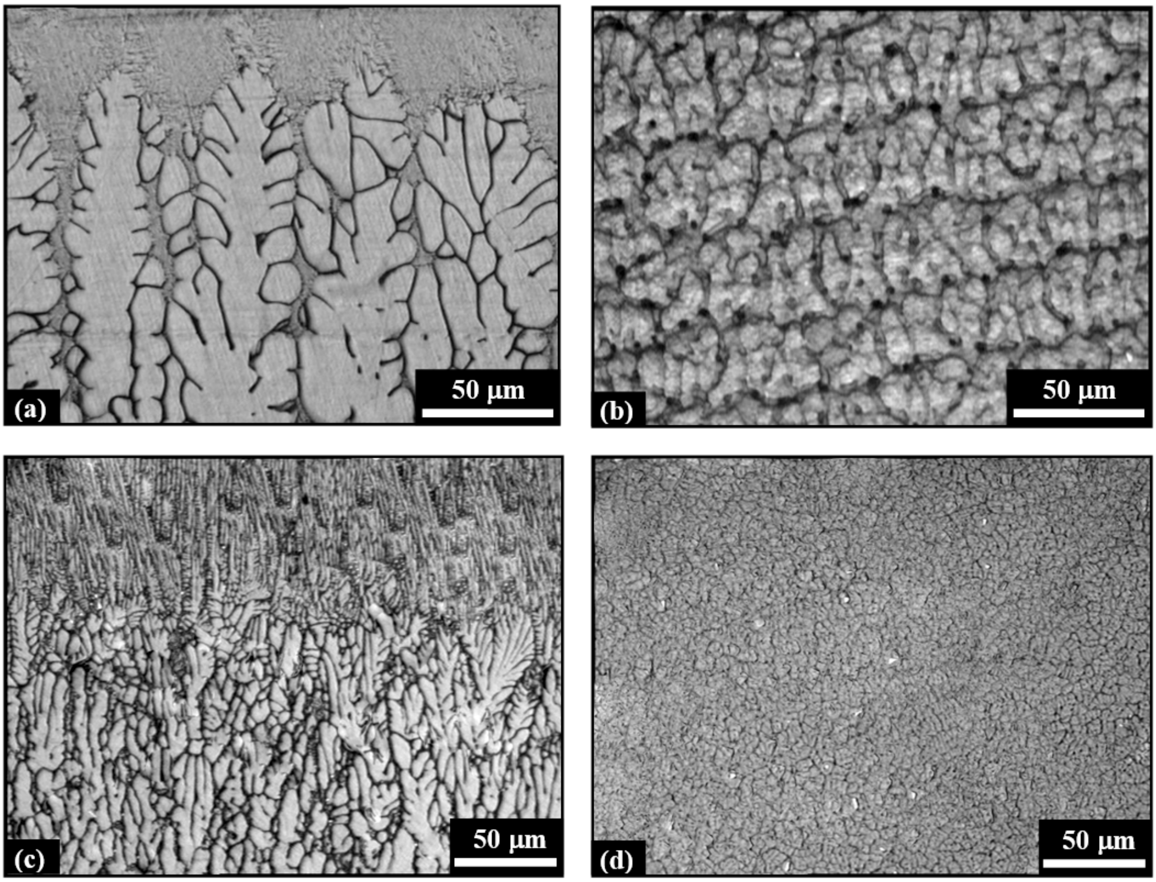

Figure 4. Microstructures of the directionally solidified Sn–10.2 Sb peritectic alloy: (a) longitudinal section; (b) transverse section (G=4.5 K. mm^{-1}, V = 26.7 µm. s^{-1}); (c) longitudinal section; (d) transverse section (G=4.5 K. mm^{-1}, V = 266.7 µm. s^{-1})

Table 1. The relationships between the dendritic spacings (λ_1, λ_2), mechanical properties (HV_L, HV_T, σ_c) and the growth velocity (V)

Relationship	Constant (k)	Correlation coefficient (r)
$\lambda_{1L} = k_1 V^{-0.24}$	k_1=153.7 (µm$^{1.24}$. s$^{-0.24}$)	r_1 = -0.998
$\lambda_{1T} = k_2 V^{-0.25}$	k_2=152.3 (µm$^{1.25}$. s$^{-0.25}$)	r_2 = -0.997
$\lambda_2 = k_3 V^{-0.46}$	k_3=158.5 (µm$^{1.43}$. s$^{-0.43}$)	r_3 = -0.994
$HV_L = k_4\ V^{-0.09}$	k_4=25.6 (kg. mm$^{-2.09}$. s$^{-0.09}$)	r_4 = -0.991
$HV_T = k_5\ V^{-0.08}$	k_5=23.3 (kg. mm$^{-2.08}$. s$^{-0.08}$)	r_5 = -0.996
$\sigma_c = k_6\ V^{-0.10}$	k_6=63.1 (MPa. µm$^{0.10}$. s$^{-0.10}$)	r_6 = -0.978

λ_{1L}: the values of the PDAS measured from the longitudinal section of the samples; λ_{1T}: the values of the PDAS measured from the transverse section of the samples; λ_2: the values of the SDAS measured from the longitudinal section of the samples; HV_L: the values of the microhardness measured from the longitudinal section of the samples; HV_T: the values of the microhardness measured from the transverse section of the samples; σ_c: the values of the compressive strength measured from the longitudinal section of the samples

by Yang et al.[33], Lapin et al.[34], Kloosterman and Hosson[35], Pryds et al.[36], Gündüz et al.[37], and Şahin et al.[38] respectively. These exponent values are also in agreement with the value 0.25 predicted by Hunt[39], Kurz,Fisher[40] and Trivedi[41] theoretical models for steady state conditions. On the other hand, our exponent values (0.24 and 0.25) are less than the values of 0.40 and 0.41 obtained by Miyata et al.[42] and Jesse,Giller[43] and also the 0.50 predicted by Kurz et al., [44] numerical models for dendritic spacings. This discrepancy might be due to rapid solidification conditions for the numerical model[44], because under rapid solidification conditions, m (liquidus slope) and k (distribution coefficient) cannot be constant and k becomes a function of growth velocity.[45] As can be seen from the theoretical and numerical models, coefficients of λ_1 and λ_2 are functions of m and k. Thus, the rapid solidification and unsteady conditions cannot apply to steady state conditions case.

The exponent value (0.46) of λ_2 is in good agreement with the values 0.42 and 0.47 obtained by Şahin et al.[38] and Kaya et al.[46] respectively. In the present work, the λ_2 values experimentally obtained as a function of growth velocity have been compared with the values of λ_2 calculated from the Trivedi–Somboonsuk[47] and the Bouchard–Kirkaldy[48,49] models. Our experimental values agree with the calculated

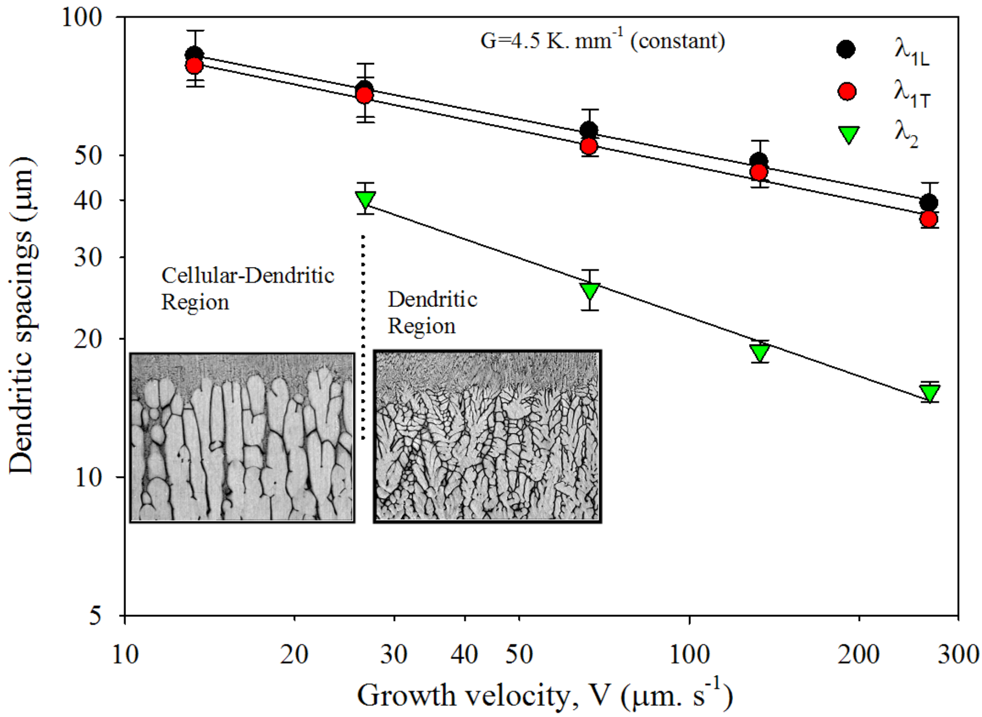

Figure 5. The variation of PDAS and SDAS with growth velocity at a constant temperature gradient

values of λ_2 from the Trivedi–Somboonsuk steady state model[47] as a function of $(V)^{0.5}$. In contrast, the calculated values of λ_2 with the Bouchard–Kirkaldy unsteady state model[48,49] as a function of $V^{0.67}$ do not agree with our experimental values. There is a clear difference between the exponent values obtained in the Trivedi–Somboonsuk and the Bouchard–Kirkaldy models. Briefly, the results of our experiments (which were carried out under steady state conditions), agree with the results of the steady state theoretical models.

3.3. The Effect of growth velocity on microhardness and compressive strength

The high microhardness and compressive strength are reported to arise from the dendritic matrix due to Hall–Petch-type mechanism[50,51]. The Hall–Petch-type relationships between the growth velocity (V) and mechanical properties (HV, σ_c), can be expressed as follows,

$$HV_L = k_4\ V^{-d} \quad (3a)$$

$$HV_T = k_5\ V^{-e} \quad (3b)$$

$$\sigma_c = k_6\ V^{-f} \quad (4)$$

where d, e and f are the exponent values relating to the V and the k_4, k_5 and k_6 are constants which can be experimentally determined (Table 1). According to Eqs. (3) and (4), the microhardness and compressive strength change with the growth velocity. At a constant temperature gradient (4.5 K/mm), an increase in the growth velocity resulted in increased microhardness (Figure 6). When the growth velocity was increased from 13.3.3 to 266.7 μm. s^{-1}, the HV_L increased from 16.8 to 21.7 kg. mm^{-2} and the HV_T increased from 18.1 to 23.3 kg. mm^{-2}. The exponent value of V (0.08) obtained from this study as a function of HV is in agreement with the values of 0.06, 0.06, 0.07 and 0.09 reported by Çadırlı et al.[52] for Sn-23Bi- 5Zn (wt%) alloy, by Hu et al.[53] for Sn-58 wt% Bi eutectic alloy, by Vnuk et al.[54] for Sn–Zn eutectic alloy, and by Böyük and Maraşlı[55] for Sn-3.5Ag-0.9Cu (wt%) eutectic alloy respectively. The exponent value of V (0.08) is slightly lower than the values of 0.11 reported by Hu et al.[56] for Sn-1.0 wt% Cu.

As seen in Figure 7(a), compressive strength (σ_c) values increased with increasing V, but strain (%) values decreased. The maximum compressive strength of studied alloy reaches 107 MPa (Figure 7(b)). The factor responsible for higher compressive strength in the investigated alloys is fineness of the dendritic and SnSb intermetallic phases. Similar trends were observed by some researchers for different multicomponent alloys[57-59]. It can be seen from these figures that the σ_c values increased by approximately 36% with increasing V for the studied alloy. The exponent value of V is equal to 0.10. This exponent value is smaller than the values of 0.20 and 0.23 obtained by Siewert et al.,[60,61] for some soldering alloys. These discrepancies are due to factors such as composition, temperature gradient, microsegregation and presence of intermetallic phases.

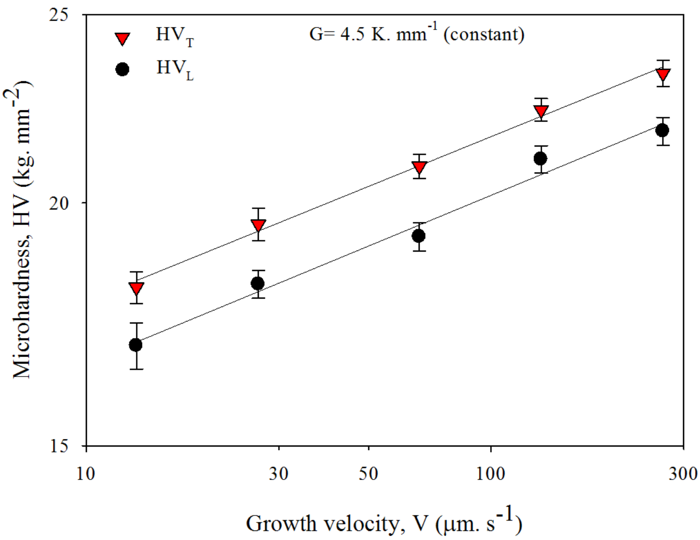

Figure 6. The variation of microhardness with growth velocity at a constant temperature gradient

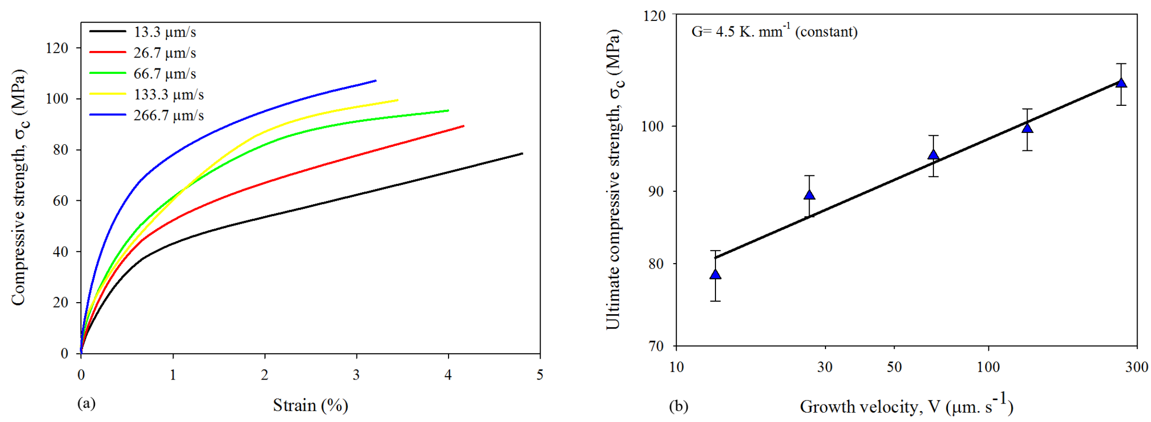

Figure 7. (a) Compressive strength-strain curve (b) the variation of ultimate compressive strength with growth velocity at a constant temperature gradient

4. Conclusions

In this work, microstructural properties of the directionally solidified Sn–10.2 Sb peritectic alloy were investigated. The results are summarized as follows:

(1) The effects of growth velocity on PDAS and SDAS were investigated. Increasing of growth velocity was observed to result in finer microstructures.

(2) Experimental relationships $\lambda_{IL} = k_1\ V^{-0.24}$, $\lambda_{IT} = k_2\ V^{-0.25}$ and $\lambda_2 = k_3\ V^{-0.46}$ show that the dependency of the λ_2 on growth velocity is stronger than λ_1.

(3) The exponent values (0.24 and 0.25) obtained in this experimental study for PDAS and SDAS are in agreement with the exponent value (0.25) predicted by theoretical models[39-41,47] for the steady state conditions. However , Kurz–Giovanola–Trivedi[44] for rapid solidification conditions (for λ_1) and Bouchard–Kirkaldy models[48,49] for the unsteady state conditions (for λ_2) do not agree with the experimental results.

(4) Increasing of growth velocity resulted in finer dendritic microstructures, thereby resulting in increased microhardness and compressive strength. The establishment of the relationships between HV_L, HV_T, σ_c and V have been obtained as $HV_L=k_4V^{-0.09}$, $HV_T=k_5\ V^{-0.08}$ and $\sigma_c=k_6V^{-0.10}$

Acknowledgements

This project was financially supported by the Erciyes University Scientific Research Project Unit under contract No: FBT–07–18.

References

1. Kerr HW, Kurz W. Solidification of peritectic alloys. *International Materials Reviews*. 1996; 41(4):129−164. DOI: 10.1179/095066096790151231
2. Trivedi R, Park JS. Dynamics of microstructure formation in the two-phase region of peritectic systems. *Journal of Crystal Growth*. 2002;235(1-4):572−588.
3. Trivedi R, Shin JH. Modelling of microstructure evolution in peritectic systems. *Materials Science and Engineering A*. 2005;413−414:288−295. DOI: 10.1016/j.msea.2005.09.027
4. Hu X, Li S, Liu L, Fu H. Microstructure evolution of directionally solidified Sn-16%Sb hyperperitectic alloy. *China Foundry*. 2008;5:167−171.
5. Wei Z, Bingbo W. Peritectic solidification characteristics of Sb–Sn alloy under ultrasonic vibration. *Materials Letters*. 2015;138:1–4.
6. Şahin M, Çadırlı E. The effect of temperature gradient and growth rate on the microstructure of directionally solidified Sn-3.5Ag eutectic solder. *Journal of Material Science: Materials in Electronics*. 2012;23(2): 484−492.
7. Çadırlı E, Kaya H, Boyuk U, Maraşlı N. Effects of solidification parameters on the microstructure of directionally solidifed Sn-Bi-Zn lead-free solder. *Metals and Materials International*. 2012;18(2):349−354. DOI 10.1007/s12540-012-2021-7
8. Ma D, Li Y, Ng SC, Jones H. Unidirectional solidification of Zn-rich Zn-Cu peritectic alloys-II. Microstructural length scales. *Acta Materialia*. 2000;48:1741−1751. DOI: 10.1016/S1359-6454(00)00003-3
9. Su Y, Wang M, Lin X, Huang W. Researches on lamellar structures in the unidirectional solidification Zn-2wt.%Cu peritectic alloy. *Materials Letters*. 2004;58(21):2670−2674.
10. Xu W, Ma D, Feng YP, Li Y. Observation of lamellar structure in a Zn-rich Zn-6.3at.%Ag hyper-peritectic alloy processed by rapid solidification. *Scripta Materialia*. 2001; 44(4):631−636.
11. Su Y, Liu C, Li X, Guo J, Li B, Jia J, Fu H. Microstructure selection during the directionally peritectic solidification of Ti-Al binary system. *Intermetallics*. 2005;13(3-4): 267−274.
12. Lee JH, Verhoeven JD. Peritectic formation in the Ni-Al system. *Journal of Crystal Growth*. 1994;144(3):353−366. DOI: 10.1016/0022-0248(94)90477-4
13. Gigolottia JCJ, Suzuki PA, Nunes CA, Coelho GC. Microstructural characterization of as-cast Hf–B alloys. *Materials Research*. 2012;15(2):185−190.
14. Rao Q, Fan X, Shu D, Wu CC. In-situ XRD study on the peritectic reaction of YBCO thin film on MgO substrate. *Journal of Alloys and Compounds*. 2008;461:L29−L33.
15. Zhong H, Li S, Lu H, Liu L, Zou G, Fu H. Microstructure evolution of peritectic Nd14Fe79B7 alloy during directional solidification. *Journal of Crystal Growth*. 2008; 310(14):3366−3371.
16. Su Y, Guo J, Li X, Li S, Zhong H, Liu L, Fu H. Peritectic reaction and its influences on the microstructures evolution during directional solidification of Fe-Ni alloys. *Journal of Alloys and Compounds*. 2008;461:121−127.
17. Luo L, Su Y, Li X, Guo J, Yang HM, Fu H. Producing well aligned in situ composites in peritectic systems by directional solidification. *Applied Physics Letters*. 2008;92:061903. http://dx.doi.org/10.1063/1.2841639
18. Fu JW, Yang YS, Guo JJ, Ma JC, Tong WH. Formation of a two-phase microstructure in Fe-Cr-Ni alloy during directional solidification. *Journal of Crystal Growth*. 2008;311(1): 132−136. DOI: 10.1016/j.jcrysgro.2008
19. Ma D, Xu W, Ng SC, Li Y. On secondary dendrite arm coarsening in peritectic solidification. *Materials Science and Engineering A*. 2005;390:52−62.
20. Zhong H, Li S, Liu L, Lv H, Zou G, Fu H. Secondary dendrite arm coarsening and peritectic reaction in NdFeB alloys. *Journal of Crystal Growth*. 2008;311(2):420−424. DOI: 10.1016/j.jcrysgro.2008.11.047
21. Biswas K, Hermann R, Wendrock H, Priede J, Gerbeth G, Buechner B. Effect of melt convection on the secondary dendritic arm spacing in peritectic Nd–Fe–B alloy. *Journal of Alloys and Compounds*. 2009;480(2):295–298.
22. Aguiar MR, Caram R. Directional solidification of a Sn-Se eutectic alloy using the Bridgman-Stockbarger method. *Journal of Crystal Growth*. 1996;166(1):398-401. DOI: 10.1016/0022-0248(95)00524-2
23. Zhai W, Hong ZY, Mei CX, Wang WL, Wei B. Dynamic solidification mechanism of ternary Ag–Cu–Ge eutectic alloy under ultrasonic condition. *Science China Physic, Mechanics & Astronomy*. 2013;56(2):462–473. DOI: 10.1007/s11433-013-5004-x
24. Liu D, Li X, Su Y, Peng P, Luo L, Guo J, et al. Secondary dendrite arm migration caused by temperature gradient zone melting during peritectic solidification. *Acta Materialia*. 2012;60(6-7):2679–2688.
25. Jiang Z, Lu Y, Zhao S, Gu W, Zhang Z. Effect of some elements on the performance of lead–antimony alloys for lead/acid batteries. *Journal of Power Sources.* 1990;31: 169−175.
26. Xie J, Zheng YX, Pan RJ, Liu SY, Song WT, Cao GS, et al. Sb-based alloy (NiSb, FeSb2) nanoparticles decorated graphene prepared by one-step solvothermal route as anode for Li-Ion batteries. *International Journal of Electrochemical Science*. 2011;6: 4811–4821. http://www.electrochemsci.org/papers/vol6/6104811.pdf
27. Guan XF, Zhu DY, Chen LJ, Tang W. Rapid solidification of Sn-Sb peritectic alloy. *The Chinese Journal of Nonferrous Metals*. 2004;14:93−98.
28. Rosa DM, Spinelli JE, Osório WR, Garcia A. Effects of cell size and macrosegregation on the corrosion behavior of a dilute Pb–Sb alloy. *Journal of Power Sources*. 2006;162(1):696-705. DOI: 10.1016/j.jpowsour.2006.07.016
29. Chen SW, Chen CC, Gierlotka W, Zi AR, Chen PY, Wu HJ. Phase equilibria of the Sn-Sb binary system. *Journal of Electronic Materials*, 2008;37(7):992−1002. DOI 10.1007/s11664-008-0464-x
30. Gündüz M, Çadırlı E. Directional solidification of aluminium-copper alloys. *Materials Science and Engineering A*. 2002;327(2):167−185.
31. Ourdjini A Liu J, Elliott R. Eutectic spacing selection in Al–Cu system. *Materials Science and Technology*. 1994;10(4):312−318.
32. Aker A, Kaya H. Measurements of microstructural, mechanical, electrical, and thermal properties of an Al–Ni alloy. *International Journal of Thermophysics*. 2013;34(2):267-283. DOI 10.1007/s10765-013-1401-7
33. Yang S, Huang W, Lin X, Su Y, Zhou Y. On cellular spacing selection of Cu-Mn alloy under ultra-high temperature gradient and rapid solidification condition. *Scripta Materialia*. 2000;42:543−548.
34. Lapin J, Klimova A, Velisek R, Kursa M. Directional solidification of Ni-Al-Cr-Fe alloy. *Scripta Materialia*. 1997;37:85−91.
35. Kloosterman AB, Hosson JT. Cellular growth and dislocation structures in laser-nitrided titanium. *Journal of Materials Science*. 1997;32(23):6201−6205. DOI 10.1023/A:1018672707864

36. Pryds NH, Juhl TW, Pedersen AS. The solidification characteristics of laser surface-remelted Fe-12Cr-nC alloys. *Metallurgical and Materials Transactions A*. 1999;30(7): 1817−1826.DOI 10.1007/s11661-999-0180-z
37. Gündüz M, Kaya H, Çadırlı E, Maraşlı N, Keşlioğlu K, Saatçi B. Effect of solidification processing parameters on the cellular spacings in the Al-0.1wt %Ti and Al-0.5wt %Ti alloys. *Journal of Alloys and Compounds*. 2007;439(1-2):114−127. doi:10.1016/j.jallcom.2006.08.246
38. Şahin M, Çadırlı E, Kaya H. Influence of the solidification parameters on dendritic microstructures in unsteady-state directionally solidified of lead-antimony alloy. *Surface and Review Letters*. 2010;17:477−486. DOI: 10.1142/S0218625X10014326
39. Hunt JD. Cellular and primary dendrite spacings, solidification and casting of metals. In: *International Conference on Solidification. Proceedings*. London. The Metals Society: 1979. p. 3–9.
40. Kurz W, Fisher DJ. Dendrite growth at the limit of stability: tip radius and spacing. *Acta Materialia*. 1981;29(1):11–20. DOI: 10.1016/0001-6160(81)90082-1
41. Trivedi R. Interdendritic spacing: Part II. A Comparison of theory and experiment. *Metallurgical and Materials Transactions A*. 1984;15(6):977–982. DOI 10.1007/BF02644689
42. Miyata Y, Suzuki T, Uno IJ. Cellular and dendritic growth: Part I. Experiment. *Metallurgical and Materials Transactions A*. 1985;16(10):1799–1805. DOI 10.1007/BF02670367
43. Jesse RE, Giller HF. Cellular growth: The relation between growth velocity and cell size of some alloys of cadmium and zinc. *Journal of Crystal Growth*. 1970;7(3):348–352. doi:10.1016/0022-0248(70)90062-X
44. Kurz W, Giovanola B, Trivedi R. Microsegregation in rapidly solidified Ag-15wt%Cu. *Journal of Crystal Growth*. 1988;91(1-2):123–125.doi:10.1016/0022-0248(88)90376-4
45. Kurz W, Fisher DJ. *Fundamentals of solidification*. Aedermannsdorf, Switzerland Trans Tech; 1989.
46. Kaya H, Çadırlı E, Gündüz M. Dendritic growth in an aluminum-silicon alloy. *Journal of Materials Engineering and Performance*. 2007;16(1):12–21. DOI 10.1007/s11665-006-9002-2
47. Trivedi R, Somboonsuk K. Constrained dendritic growth and spacing. *Materials Science and Engineering*. 1984;65(1):65–74. doi:10.1016/0025-5416(84)90200-3
48. Bouchard D, Kirkaldy JS. Scaling of intragranuiar dendritic microstructure in ingot solidification. *Metallurgical and Materials Transactions B*. 1996;27(1):101–113.DOI 10.1007/BF02915081
49. Bouchard D, Kirkaldy JS. Prediction of dendrite arm spacings in unsteady-and steady-state heat flow of unidirectionally solidified binary alloys. *Metallurgical and Materials Transactions B*. 1997;28(4):651–663.DOI 10.1007/s11663-997-0039-x
50. Hall EO. The deformation and ageing of mild steel: discussion of results. In: *The Physical Society of London. Proceedings*. London; 1951;Section B 64:747–753.
51. Petch NJ. The cleavage strength of polycrystals. *The Journal of the Iron and Steel Institute*. 1953;174 25–28.
52. Çadırlı E, Böyük U, Kaya H, Maraşlı N. Determination of mechanical, electrical and thermal properties of the Sn-Bi-Zn ternary alloy. *Journal of Non-Crystalline Solids*. 2011; 357:2876–2881.DOI: 10.1016/j.jnoncrysol.2011.03.025
53. Hu X, Li K, Ai F. Research on lamellar structure and micro-hardness of directionally solidified Sn-58Bi eutectic alloy. *China Foundry*. 2012;9:360–365.
54. Vnuk F, Sahoo M, Baragor D, Smith RW. Mechanical properties of Sn-Zn eutectic alloys. *Journal of Materials Science*. 1980;15(10):2573–2583. DOI 10.1007/BF00550762
55. Böyük U, Maraşlı N. The microstructure parameters and microhardness of directionally solidified Sn-Ag-Cu eutectic alloy. *Journal of Alloys and Compounds*. 2009;485(1-2): 264–269.doi:10.1016/j.jallcom.2009.06.067
56. Hu X, Chen W, Wu B. Microstructure and tensile properties of Sn-1Cu lead-free solder alloy produced by directional solidification. *Materials Science and Engineering A*. 2012; 556:816–823.
57. Mondal B, Samal S, Biswas K. Development of ultrafine Ti-Fe-Sn in-situ composite with enhanced plasticity. *IOP Conference Series on Materials Science*. 2011;27:012025.
58. Samal S, Biswas K. Novel high strength $Ni_{48}Cu_{10}Co_2Ti_{38}Ta_2$ composite with enhanced plasticity. *Journal of Nanoparticle Research*. 2013;15:1783.
59. Samal S, Mohanty S, Mishra A K, Biswas K, Govind B. Microstructural evolution of ultrafine Ti-Fe-Co alloys. *Materials Science Forum*. 2014;790–791:497-501.
60. Siewert T, Liu S, Smith DR, Madeni JC. *Database for solder properties with emphasis on new lead-free solders*. Colorado: National Institute of Standards and Technology, Colorado School of Mines; 2002. http://www.msed.nist.gov/solder/NIST_LeadfreeSolder_v4.pdf
61. Siewert T, Madeni JC, Liu S. Lead free solder data collection and development. In: *Welding & Joining 2005: Frontiers of Materials Joining*. Tel Aviv, Israel; 2005.